

## Electromagnetic dissociation of relativistic $^{18}\text{O}$ nuclei

D. L. Olson and B. L. Berman

*Lawrence Livermore Laboratory, University of California, Livermore, California 94550*

D. E. Greiner, H. H. Heckman, P. J. Lindstrom, and G. D. Westfall

*Lawrence Berkeley Laboratory, University of California, Berkeley, California*

H. J. Crawford

*University of California Space Sciences Laboratory, Berkeley, California 94720*

(Received 26 February 1981)

Measurements of fragment-production cross sections have been made with  $^{18}\text{O}$  projectiles of 1.7 GeV/nucleon incident upon targets of Be, C, Al, Ti, Cu, Sn, W, Pb, and U. We have found that the enhancement with high- $Z$  targets of cross sections for certain fragments agrees both in magnitude and  $Z_T$  dependence with the predictions of the electromagnetic-dissociation process, which are based upon the known photonuclear cross sections and classical relativistic virtual-photon theory. We have found as well that factorization of the cross sections for nuclear processes is valid to an accuracy of better than 4%.

NUCLEAR REACTIONS Be( $^{18}\text{O}, X$ ), C( $^{18}\text{O}, X$ ), Al( $^{18}\text{O}, X$ ), Ti( $^{18}\text{O}, X$ ), Cu( $^{18}\text{O}, X$ ), Sn( $^{18}\text{O}, X$ ), W( $^{18}\text{O}, X$ ), Pb( $^{18}\text{O}, X$ ), U( $^{18}\text{O}, X$ ),  $X = {}^6\text{Li}$  to  $^{18}\text{F}$ ,  $E = 1.7$  GeV/nucleon; measured fragment-production cross sections; deduced electromagnetic-dissociation cross sections,  $Z_T$  dependence, factorization parameters.  $^{18}\text{O}$  fragment-production cross sections, electromagnetic dissociation, factorization, relativistic heavy ions.

### I. INTRODUCTION

There have been two previous experiments<sup>1,2</sup> in which the enhancement of fragment-production cross sections for high- $Z$  targets was compared with the predictions of electromagnetic dissociation.<sup>3</sup> For both the experiment with  $^{12}\text{C}$  and  $^{16}\text{O}$  projectiles,<sup>1</sup> where the enhancement was noticed in the single-nucleon-loss channel, and the experiment with  $^{56}\text{Fe}$  projectiles,<sup>2</sup> where the enhancement was seen in the Mn-fragment channel, the results were found to be consistent with these predictions. However, in themselves they do not constitute a compelling experimental verification of the electromagnetic dissociation of relativistic nuclei. A description of this process is given in Sec. II.

A beam of  $^{18}\text{O}$  nuclei of energy 1.7 GeV/nucleon was chosen to provide a definitive test of the electromagnetic-dissociation process. For  $^{18}\text{O}$ , in addition to the single-nucleon photonuclear channels,  $\sigma(\gamma, n)$  and  $\sigma(\gamma, p)$ , there is a large two-neutron cross section  $\sigma(\gamma, 2n)$ . All of these cross sections were measured simultaneously at the Lawrence Livermore Laboratory Electron-Positron Linear Accelerator,<sup>6</sup> which lends great significance to the comparison of the relative magnitudes of the cross sections,  $\sigma_{em}$ . Also, the large  $^{18}\text{O}(\gamma, 2n)$  cross section provides an important signature of an electromagnetic process. Finally, the magnitudes of the electromagnetic-dissociation

cross sections for  $^{18}\text{O}$  are comparable to the contributions from the competing nuclear processes.

In this experiment we measured the fragment-production cross sections for  $^{18}\text{O}$  projectiles and the targets Be, C, Al, Ti, Cu, Sn, W, Pb, and U, for fragments ranging from  ${}^6\text{Li}$  to  $^{18}\text{F}$  with rigidity  $4.8 < R < 6.3$  GV/c. These cross sections result from both nuclear and electromagnetic processes, and we take them to be of the form

$$\sigma(T, F) = \sigma_{nuc}(T, F) + \sigma_{em}(T, F) \quad (1)$$

(which assumes no interference between the nuclear and the electromagnetic processes). Because the calculated  $\sigma_{em}$  increases about 12% per fm increase in the overlap distance  $d$  (see Sec. II) and because of the high incident energy and the resulting forward trajectories, this interference is expected to be small. This is equivalent to the electromagnetic-dissociation process being dominated by higher partial waves than those for the nuclear-fragmentation process, which is clearly the case.

Essential to our analysis is the factorization of the nuclear cross section,

$$\sigma_{nuc}(T, F) = \gamma_T \gamma_F, \quad (2)$$

where  $\gamma_T$  and  $\gamma_F$  are factors which depend only upon target and fragment, respectively.<sup>7,8</sup> These factors are determined empirically from a set of  $\sigma(T, F)$ , where  $\sigma_{em}(T, F)$  is negligible. After the  $\gamma_T$  and  $\gamma_F$  have been determined they are applied

in the appropriate combination to give  $\sigma_{\text{em}}(T, F)$  from Eqs. (1) and (2).

## II. THEORETICAL BACKGROUND

### A. Calculation of cross sections

The electromagnetic dissociation of a relativistic nucleus ( $T \sim \text{GeV/nucleon}$ ) is illustrated in Fig. 1 in comparison with peripheral fragmentation caused by nuclear processes. The electromagnetic-dissociation process occurs when a projectile nucleus passes near a high- $Z$  target nucleus, but conceptually beyond the range of the nuclear force. The projectile is excited by photoabsorption in the Coulomb field of the target nucleus, and then decays by particle emission.

In this experiment, the kinetic energy of the beam,  $^{18}\text{O}$  at 1.7 GeV/nucleon, is more than two orders of magnitude greater than the Coulomb barrier for  $^{18}\text{O} + \text{U}$ , which is  $\sim 100$  MeV. As a result, the electromagnetic dissociation investigated here is dominated by transverse photons, and the interference with nuclear processes is expected to be small.

A method of calculating cross sections for this process is indicated in Fig. 2 for the reaction  $^{18}\text{O} + \text{U} \rightarrow ^{17}\text{O} + n + \text{U}$ . By taking the product of a virtual-photon spectrum,<sup>9</sup> Fig. 2(a), with the photoneutron

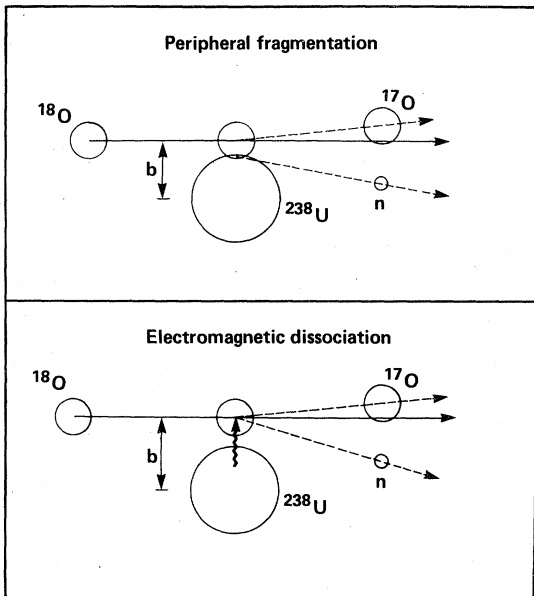


FIG. 1. Schematic diagram of the fragmentation reaction  $^{18}\text{O} + ^{238}\text{U} \rightarrow ^{17}\text{O} + n + ^{238}\text{U}$  showing the process of peripheral fragmentation resulting from the nuclear force and the electromagnetic-dissociation process occurring in the Coulomb field of the target nucleus. Note that electromagnetic dissociation can occur over a wide range of impact parameters, much larger than the limit set by the range of the nuclear force.

cross section,<sup>6</sup> Fig. 2(b), one obtains the differential-in-photon-energy cross section, Fig. 2(c). At this point it is interesting to note that the low-energy part of this cross section is greatly enhanced and the high-energy part suppressed relative to the photoneutron cross section. Finally, we integrate this differential cross section to get the total electromagnetic-dissociation cross section

$$\sigma_{\text{em}}(T, F) = \int_0^\infty N_\gamma \sigma(\gamma, n) dE_\gamma, \quad (3)$$

where  $T$  and  $F$  stand for target (U) and fragment ( $^{17}\text{O}$ ), respectively. In order to use the cross section measured with real photons in Eq. (3), we assume that the virtual-photon spectrum  $N_\gamma$  is the same for all multiplicities (see below). This is equivalent to the assumption that all of the photons are transverse.

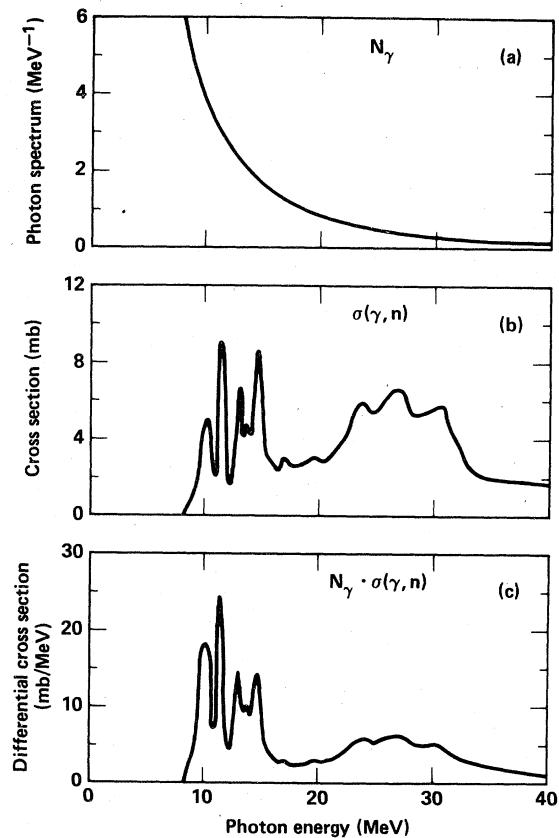


FIG. 2. Ingredients for the theoretical calculation of the electromagnetic dissociation cross section  $\sigma_{\text{em}}(\text{U}, ^{17}\text{O})$  for  $^{18}\text{O}$  at 1.7 GeV/nucleon. Part (a) shows the E1 virtual-photon spectrum  $N_\gamma$  ( $d$ ) of Ref. 9 for  $d = 1.5$  fm ( $b_{\text{min}} = 10.2$  fm). Part (b) shows the measured photoneutron cross section  $\sigma(\gamma, n)$  for  $^{18}\text{O}$ , from Ref. 6. Part (c) is the product  $N_\gamma \cdot \sigma(\gamma, n)$ , which is the differential-in-photon-energy electromagnetic-dissociation cross section. This is integrated to produce  $\sigma_{\text{em}}(\text{U}, ^{17}\text{O})$ .

### B. Remarks on photon spectra

The two virtual-photon theories that we use are the Weizsäcker-Williams method of virtual photons from Jackson<sup>10</sup> and a more sophisticated version of this method by Jäckle and Pilkuhn,<sup>9</sup> who derive spectra for various multipolarities. The spectrum from Jackson is indicated by WW and is derived with the assumption of a point-charge target. The spectra from Jäckle and Pilkuhn are derived with the assumption of the target having a Yukawa charge distribution, and the resulting E1 and M1 spectra are indicated by JPE1 and JPM1, respectively. The spectrum from Jäckle and Pilkuhn for the case when the charge distribution of the target is taken to be a point charge<sup>11</sup> is indicated by JPJ and ought to be equivalent to WW;

$$N_{\text{WW}} = \frac{Z_T^2 \alpha}{\omega \beta^2} \left[ q_i R K_{10} K_{11} - \frac{1}{2} \beta^2 q_i^2 R^2 (K_{11}^2 - K_{10}^2) \right],$$

$$N_{\text{JPE1}} = \frac{Z_T^2 \alpha R^2}{\pi \omega^3} \left\{ q_i^2 q_L^2 \left( K_{10} K_{12} - K_{11}^2 - 2K_{L0} \frac{K_{12} - K_{10}}{1 - a^2 \omega^2} \right) + q_i^4 (K_{11}^2 - K_{10}^2) + (q_L^4 + a^4 \omega^4 c^4) \frac{K_{c1}^2 - K_{c0}^2}{(1 - a^2 \omega^2)^2} \right. \\ \left. + q_L^2 c^2 (1 + a^4 \omega^4) \frac{K_{c0} K_{c2} - K_{c1}^2}{(1 - a^2 \omega^2)^2} + \frac{4}{R} q_L^3 \frac{K_{L0} - K_{c0}}{(1 - a^2 \omega^2)^2} K_{L1} \right. \\ \left. + \frac{4}{R} c a^2 \omega^2 \left[ q_i^2 K_{10} K_{c1} + c q_i \omega^2 a^2 \frac{K_{c0} K_{11}}{1 - a^2 \omega^2} - q_L^2 \frac{K_{L0} K_{c1}}{(1 - a^2 \omega^2)^2} \right] \right\},$$

$$N_{\text{JPM1}} = \frac{Z_T^2 \alpha}{\pi \omega} R^2 \left[ q_i^2 (K_{10} K_{12} - K_{11}^2) + c^2 (K_{c0} K_{c2} - K_{c1}^2) - 4 \frac{c}{R} q_i a^2 (c K_{c0} K_{11} - q_i K_{10} K_{c1}) \right],$$

and for  $N_{\text{JPJ}}$  ( $a=0$ ,  $c \rightarrow \infty$ ) we have

$$N_{\text{JPJ}} = \frac{Z_T^2 \alpha R^2}{\pi \omega^3} \left\{ q_i^2 q_L^2 [K_{10} K_{12} - K_{11}^2 - 2K_{L0} (K_{12} - K_{10})] \right. \\ \left. + q_i^4 (K_{11}^2 - K_{10}^2) + \frac{4}{R} q_L^3 K_{L0} K_{L1} \right\}.$$

These spectra are shown in Fig. 3 for several beam energies. The following discussion will focus on the set for  $10^3$  MeV/nucleon in the region  $10 < E_\gamma < 30$  MeV, which corresponds to the case most applicable to our experiment. One can see that  $N_{\text{JPE1}}$  (curve *b*) and  $N_{\text{JPM1}}$  (curve *c*) differ by about 10%. This, combined with the dominance of E1 transitions in the photonuclear cross sections, means that the assumption of equal multipolarities in Eq. (3) is quite good; the uncertainty introduced into the calculated  $\sigma_{\text{em}}$  by this assumption is less than the uncertainty in the measured photonuclear cross sections. Another feature to be noted is that  $N_{\text{JPJ}}$  (curve *d*) is nearly identical to  $N_{\text{JPE1}}$ , differing by  $\approx 1\%$ . This means that the size of the charge distribution in the target is of little importance. A bothersome feature is that  $N_{\text{WW}}$  (curve *a*) is larger than  $N_{\text{JPE1}}$  by 30–40%. Since this experiment is not sensitive to the exact shape of the photon

however, it is not.

These spectra have one free parameter,  $b_{\text{min}}$ , which is the minimum impact parameter for the process. In our case, this is the impact parameter for which nuclear processes cease to dominate the interaction, and is the sum of the matter radii of the beam and target nuclei.

We simply quote the formulas for these spectra where  $Z_T$  is the charge of the target,  $\gamma$  and  $\beta$  are the usual relativistic factors,  $\omega$  is the photon energy,  $q_L = \omega/\beta$ ,  $q_i = \omega/\gamma\beta$ ,  $R = b_{\text{min}}$ , the parameter for the Yukawa charge distribution is  $a = \langle r_T^2 \rangle^{1/2} / \sqrt{6}$ ,  $c^2 \equiv 1/a^2 + q_i^2$ , and  $N$  is the photon spectrum in  $\text{MeV}^{-1}$ . The modified Bessel functions are denoted by  $K_{Li} = K_i(q_L R)$ ,  $K_{1i} = K_i(q_i R)$ , and  $K_{ci} = K_i(cR)$ . With this notation, the spectra are

spectrum, the only effect of this difference is to shift the value of  $b_{\text{min}}$  by  $\sim 3$  fm. This does not impair the main feature of our experiment; nevertheless, some work on the virtual-photon theory of relativistic nuclei is clearly needed.

These spectra have a factor  $Z_T^2$ , which gives the resulting electromagnetic-dissociation cross sections a strong dependence upon the charge of the target. However, there is some dependence upon  $Z_T$  in the parameter  $b_{\text{min}}$ , since a smaller value for  $Z_T$  yields a smaller value of  $b_{\text{min}}$ . As in Ref. 1 we define the overlap distance  $d$  by

$$b_{\text{min}} = R_{0.1}(B) + R_{0.1}(T) - d, \quad (4)$$

where  $B$  stands for beam and  $R_{0.1}$  is the 10% charge-density radius. The 10% charge-density radii that we used in our calculations are listed in Table I. We expect  $R_{0.1}$  to approximate the range of the nuclear interaction at these energies. By using  $d$  for our free parameter in place of  $b_{\text{min}}$  and calculating cross sections for a variety of targets with  $d$  held constant, we find the overall target dependence of  $\sigma_{\text{em}}$  to be

$$\sigma_{\text{em}}(T, F) = Z_T^{-1.8} S(F, d), \quad (5)$$

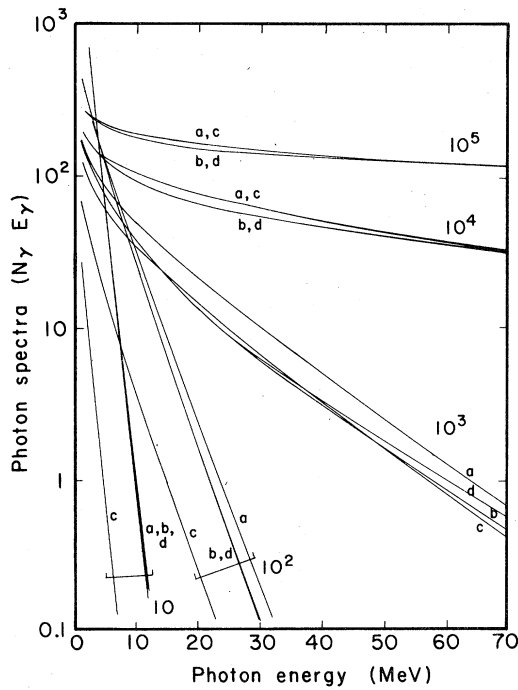


FIG. 3. Virtual-photon spectra. The sets of curves are labeled according to beam energy, from 10 to  $10^5$  MeV/nucleon. These are calculated for a U target with  $b_{\min} = 11.6$  fm. Curve a is from Ref. 10, which we denote as WW. Curves b, c, and d, from Refs. 9 and 11, are the E1, M1, and E1 (point charge) spectra which we denote as JPE1, JPM1, and JPJ, respectively.

TABLE I. Nuclear charge radii.<sup>a</sup>

	$A_T$	$R_{0.1}$ (fm)	$R_{0.1}A_T^{-1/3}$ (fm)
Target <sup>b</sup>			
Be	9.01	3.38	1.62
C	12.01	3.29	1.44
Al	26.98	4.14	1.38
Ti	47.90	4.97	1.37
Cu	63.55	5.38	1.35
Sn	118.69	6.42	1.31
W	183.85	7.35	1.29
Pb	207.20	7.73	1.31
U	238.00	7.92	1.28
Beam <sup>c</sup>			
$^{18}\text{O}$	18.0	3.74	1.43

<sup>a</sup>The nuclear skin thickness  $\equiv R_{0.1} - R_{0.9}$  is typically 2.2 fm.

<sup>b</sup> $R_{0.1}$  obtained from Ref. 12 except for Be, Ti, and Sn, for which  $R_{0.1}$  was obtained by normalizing  $\langle r^2 \rangle^{1/2}$  from Ref. 13, with  $r = 1.34, 1.38,$  and  $1.38,$  respectively.

<sup>c</sup> $R_{0.1}$  from Ref. 14.

where  $S(F, d)$  contains all of the dependence upon the fragmentation channel and the effective range of the nuclear processes.

### III. EXPERIMENTAL METHOD

The beam of  $^{18}\text{O}$  accelerated by the Lawrence Berkeley Laboratory Bevalac to 1.7 GeV/nucleon was incident upon the target in the spectrometer shown schematically in Fig. 4. The target box,

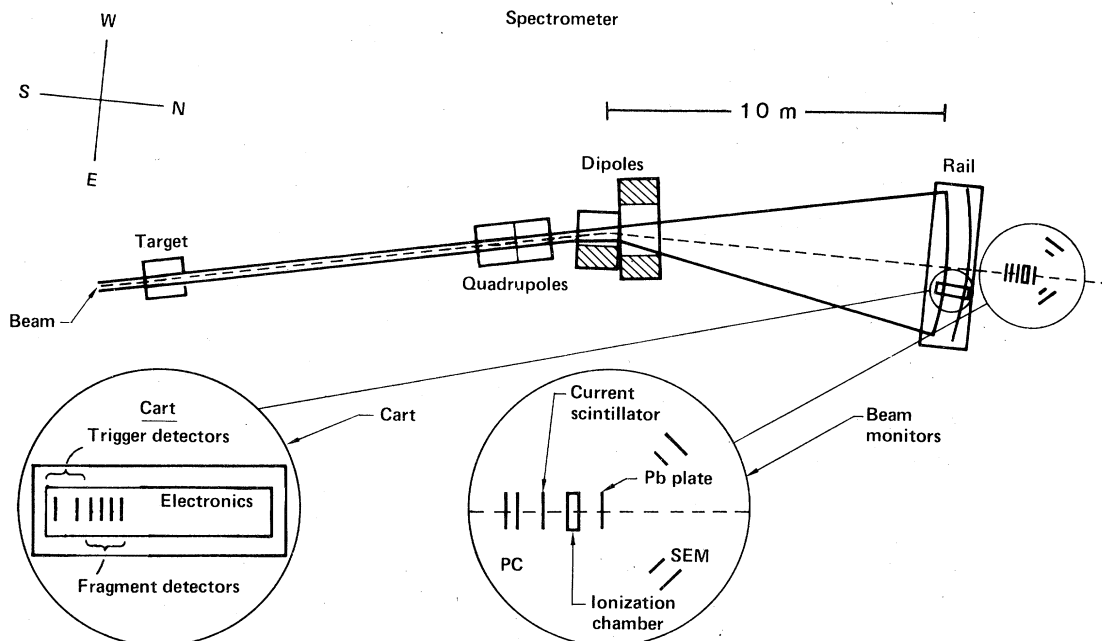


FIG. 4. Spectrometer layout. The telescope-detector cart was movable along the 4-m-long rail. Fragments were focused at the front of the telescope detector. Secondary-emission monitors were below the plane defined by the beam and the detected fragments.

at one focal point, held the nine thin 10.16-cm-diameter targets, whose characteristics are specified in Table II. The quadrupoles were used to focus fragments of the correct rigidity at the front of the detector telescope. The dipoles were set so that the unscattered  $^{18}\text{O}$  beam itself was deflected to the center of the "rail" upon which the detector-telescope cart runs.

The detector telescope consisted of two Si(Li) wafers 0.2 mm thick by 45 mm in diameter by four thick Si(Li) detectors 5 mm thick by 44 mm in diameter. The two thin detectors were operated in coincidence for the event trigger with the thresholds set to allow fragments with charge  $Z_F \geq 2$ . The four thick detectors were used to measure  $\Delta E$ , and hence the charge ( $\Delta E \propto Z_F^2$ ), of each fragment. All six of these detectors were coaxial.

The monitoring of the beam was carried out by the use of three detectors plus a lead plate in the beam line behind the path of the cart and the two secondary-emission monitors set off at  $\pm 45^\circ$  to the side of and below the beam and viewing the lead plate. The primary low-rate monitor was the particle-mode counter (PC) in the beam. It was a pair of scintillator paddles operated in coincidence which counted every beam particle for flux  $< 10^6$  per one-second beam spill. The primary high-rate monitor was the east secondary-emission monitor (SEM). This also was a pair of scintillator paddles operated so that they would have a coincidence for particles originating at the lead plate. The SEM was used for the monitor for flux  $> 10^6$  per one-second beam spill and was calibrated against the PC at low rates. The other two detectors in the beam were an ionization chamber and a current-mode scintillator. These were used for cross checks of the other monitors and gave no indication that any problem developed with either the PC or the SEM. All of the scintillator paddles were 0.64 cm thick, and the PC and the

SEM each had a scaler which was gated with the same "LIVE" signal as the charge-measuring telescope detectors.

On-line data acquisition was achieved through a CAMAC interface to a PDP 11/40 where the data were written first on a disk and then on a magnetic tape. The telescope detector was placed at 5-cm intervals over a range of 50 cm on the rail, symmetric about the beam position. There were roughly 30 000 events per run for the targets Be, C, Al, Ti, Pb, and U at each of the detector locations. The data for the targets Cu, Sn, and W were collected for only one value of rigidity, corresponding to the  $Z_F/A_F = \frac{1}{2}$  fragments.

#### IV. DATA ANALYSIS AND UNCERTAINTIES

The procedure for data reduction was to (a) calibrate the detectors for fragment charge, (b) calibrate the beam monitors, (c) compute the differential (in momentum) cross sections, (d) fit these cross sections with a Gaussian form in order to get the fragment-production cross sections, (e) correct for the transmission loss through the spectrometer in order to get the final values for  $\sigma(T, F)$ , (f) determine the factors  $\gamma_T$  and  $\gamma_F$ , and (g) derive the values for  $\sigma_{em}(T, F)$ .

##### A. Detector calibrations

Because the data were collected on an event-by-event, spill-by-spill, run-by-run basis, the calibrations could be made after the fact. Samples of data from throughout the experiment were analyzed to determine the charge calibration for each of the four thick Si(Li) detectors. The charge-identification procedure is illustrated in Fig. 5 for the  $Z/A = \frac{1}{2}$  fragments. Fig. 5(a) shows an example of a pulse-height spectrum. This spectrum was converted to a charge spectrum, shown in Fig. 5(b), using a calibration of the form

$$Z_i = C_i(D_i - D_{0i})^{1/2}, \quad (6)$$

where  $D_i$  is the analog-to-digital converter (ADC) output of the  $i$ th detector for the event,  $C_i$  and  $D_{0i}$  are the calibration constants for the detector  $i$ , and  $Z_i$  is the calculated charge of the fragment. The constants  $C_i$  and  $D_{0i}$  exhibited no time dependence during the course of the experiment. In order to minimize the misidentification of fragments resulting from interactions in the detectors, the fragment-counting procedure required that each of the four detectors measured the same integer charge. Figure 5(c) shows a spectrum of the average of the calculated charges of the four detectors when this requirement is imposed. The systematic uncertainty introduced into the final cross sections by this calibration [Eq. (6)] is  $< 1\%$ .

TABLE II. Target specifications.<sup>a</sup>

Target	$Z_T$	$A_T$	$\text{g/cm}^2$	Thickness radiation lengths <sup>b</sup>
Be	4	9.01	0.339	0.0052
C	6	12.01	0.253	0.0059
Al	13	26.98	0.328	0.014
Ti	22	47.90	0.348	0.021
Cu	29	63.55	0.425	0.033
Sn	50	118.69	0.419	0.048
W	74	183.85	0.488	0.072
Pb	82	207.2	0.570	0.089
U	92	238.0	0.587	0.098

<sup>a</sup>All targets were 10.16 cm in diameter.

<sup>b</sup>From Particle Data Group, Lawrence Berkeley Laboratory Report No. LBL-100, 1978, p. 21.

The correction for proper counting of the fragments that do not pass the requirement mentioned above will be discussed below with the cross-section formula.

The beam monitors were investigated and the SEM was determined to be the most reliable high-rate monitor. It was calibrated using the PC with beam spills having less than  $10^6$  PC counts. The dependence of PC/SEM upon target and detector

position (focusing) was investigated and no systematic target dependence was found. Therefore, the final calibration was averaged over runs with different targets at the same position, but was determined separately for each individual position. The systematic uncertainty resulting from this procedure is  $\sim 3\%$ .

### B. Differential cross section

The differential cross section (in parallel momentum) is given by

$$\frac{d\sigma}{dp} = \frac{N(Z)(A/S_N)[(N_{\text{evt}} + n_p)/N_{\text{evt}}]}{\text{SEM}(\text{PC}/\text{SEM})X_T N_T \Delta P}, \quad (7)$$

where  $N(Z)$  is the number of fragments of charge  $Z$  that had the same integer charge in each of the four detectors;  $A$  is the number of fragments whose average calculated charge is  $> 2.5$ ;  $S_N = \sum_{Z=3}^{\infty} N(Z)$ ;  $N_{\text{evt}} + n_p$  is the number of event triggers;  $n_p$  is the number of pileup events, i.e., the number of events where a second event trigger occurred before the computer had finished reading the detectors and the "LIVE" signal returned; SEM is the number of counts from the secondary-emission monitor SEM; PC/SEM is the calibration of the SEM with respect to the particle counter PC;  $X_T$  is the correction for beam loss in the target ( $1 + \leq 0.005$ );  $N_T$  is the target thickness in atoms/cm<sup>2</sup>; and  $\Delta P$  is the momentum width of the detector. Uncertainties in the term  $(N_{\text{evt}} + n_p)/N_{\text{evt}} X_T N_T \Delta P$  introduce  $\sim 1\%$  uncertainty into the cross section. The pileup correction usually was  $< 10\%$ , and thus introduces negligible uncertainty. The principal uncertainties here arise from the correction for proper fragment counting and from the beam-monitor calibration. As mentioned above, PC/SEM has  $\sim 3\%$  systematic uncertainty, independent of fragment charge, while the term  $A/S_N$  might conceivably have a  $Z$ -dependent uncertainty. The purpose of the quantity  $A/S_N$  is to normalize  $N(Z)$  to the actual number of charge- $Z$  fragments (its value is typically 1.3). The value used for  $A/S_N$  can err in two ways. First, when the number of light fragments, e.g.,  $Z=2, 3$ , or 4, is a large fraction of the total number, any charge misidentification that results from interactions in the detectors or from electronic noise might cause  $A$  to differ from the correct number of events with  $Z \geq 3$ . The uncertainty in  $d\sigma/dp$  introduced by this depends upon the relative numbers of fragments, but typically is  $\sim 1\%$  for  $Z \geq 5$  fragments,  $\sim 2\%$  for the Be fragments, and  $\sim 3\%$  for  ${}^7\text{Li}$  fragments. Second, an uncertainty in  $A/S_N$  comes about from the  $Z$ -dependent interaction rate in the detector (from geometrical considerations alone). This results in a higher efficiency

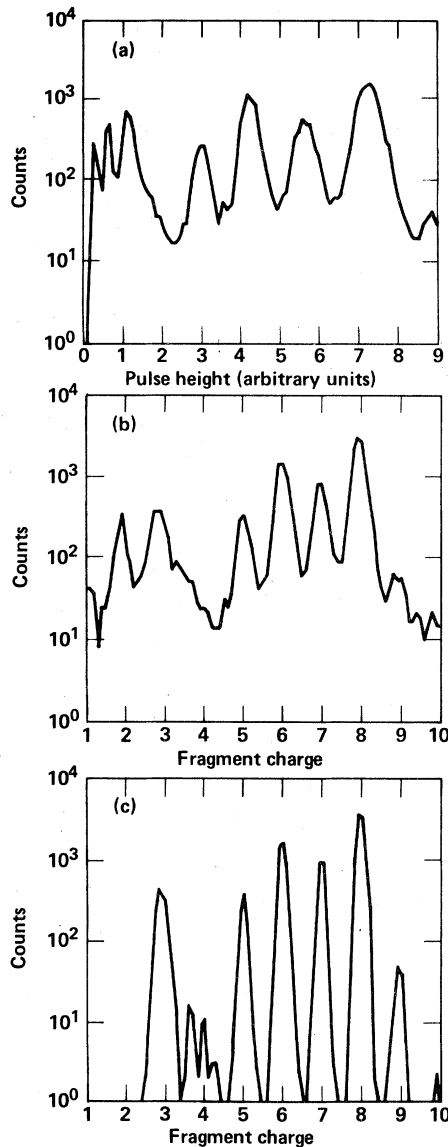


FIG. 5. Fragment-charge calibration. Part (a) shows a sample pulse-height spectrum from the leading 5-mm thick telescope detector. Part (b) shows the charge spectrum for the same data set. Part (c) shows the spectrum of the average charge measured by each of the four detectors with the requirement imposed that each detector measure the same integer charge.

for counting low- $Z$  fragments in determining  $N(Z)$  than for counting high- $Z$  fragments. However, any electronic noise or base-level fluctuations in the detectors would cause more losses for low- $Z$  fragments than for high- $Z$  fragments because the pulse-height range for each charge unit is proportional to  $Z_F^2$ . Analysis of the data yielded no noticeable  $Z$  dependence in the counting efficiency of  $N(Z)$  greater than 5%, and since  $A/S_N$  is weighted by the count rate for a given charge, it is more accurate at the peak of a differential cross section than in the tails of the distribution. The result of this uncertainty in  $A/S_N$  is an uncertainty in the total cross section of  $\sim 3\%$ .

### C. Total cross section

The differential cross sections were fitted by a least-squares minimization procedure using a Gaussian form<sup>15</sup> in parallel momentum,

$$\frac{d\sigma}{dp} = \frac{\sigma_m(T, F)}{\sqrt{2\pi}\Gamma} \exp[-(P - \langle P \rangle)^2/2\Gamma^2], \quad (8)$$

a typical example of which is shown in Fig. 6. In many cases two cross sections were fitted simultaneously, as in Fig. 6. The fitting interval never spanned the range of rigidity which included that of the beam. The fitting parameters are (a) the measured total fragment-production cross section  $\sigma_m(T, F)$ , (b) the momentum width of the distribution  $\Gamma$ , and (c) the mean momentum of the

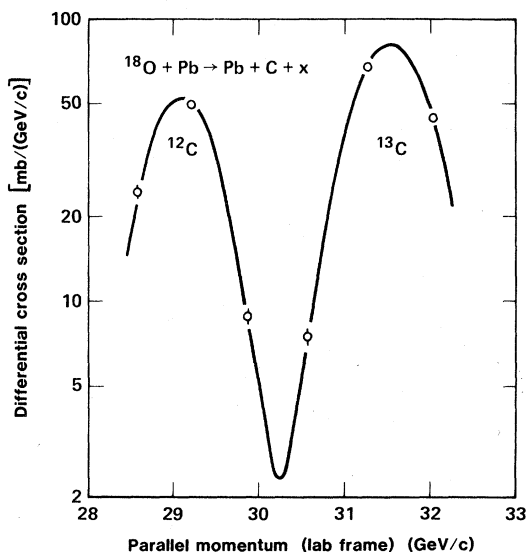


FIG. 6. A typical two-Gaussian fit of the differential (in parallel lab momentum) fragment-production cross section for the  $^{12}\text{C}$  and  $^{13}\text{C}$  fragments of  $^{18}\text{O}$  projectiles incident upon the Pb target. This fit has  $\chi^2 = 3$  for two degrees of freedom. The uncertainties indicated are statistical only. Systematic uncertainties are discussed in the text.

distribution  $\langle P \rangle$ . This last parameter,  $\langle P \rangle$ , was constrained to be the same for each of the targets and depends only upon the fragment, except for the  $^{16}\text{O}$  and  $^{17}\text{O}$  fragments. For the  $^{16}\text{O}$  and  $^{17}\text{O}$  fragments, only  $\langle P \rangle$  was constrained for the Be, C, Al, and Ti targets, while both  $\Gamma$  and  $\langle P \rangle$  were constrained for the Pb and U targets; these latter constraints were independent of those for the set of light targets. This separation of Pb and U from the Be, C, Al, and Ti targets for the case of  $^{16}\text{O}$  and  $^{17}\text{O}$  resulted in a lower  $\chi^2$  for these fits and thus allowed us to take account of any possible influence of the electromagnetic-dissociation process on  $\Gamma$  and  $\langle P \rangle$ .

There is a systematic error in this fitting procedure in addition to the unknown (and presumably small) error in the assumption that these distributions are truly Gaussian. This error owes its origin to the significant momentum interval accepted by the detector, which has the effect of distorting the distribution. This was investigated and found to have a first-order effect on the measured width  $\Gamma$  but only a second-order effect on the total cross section  $\sigma_m(T, F)$ . This distortion is greatest for the heavy fragments, and could cause  $\sigma_m(T, F)$  to be overestimated by 2–3% for  $A_F \geq 16$ , but its effect is less than 1% for  $A_F \leq 15$ .

Because of the narrow fitting interval used for the  $^6\text{Li}$ -production cross sections and the fragment-counting correction mentioned above, the  $^6\text{Li}$ -fragment cross sections contain a 20% target-dependent systematic uncertainty. There were several cases for which there were not enough data to obtain the total cross sections from this fitting procedure. These are the  $Z/A = \frac{1}{2}$  fragments for the Cu, Sn, and W targets and the  $^{16}\text{N}$  fragment for the rest of the targets (because of the proximity of the rigidity of the  $^{16}\text{N}$  to that of the beam itself). For these cases, the transformation from a single  $d\sigma/dp$  datum to the total cross section  $\sigma_m(T, F)$  was obtained by analyzing the target dependence of the ratio  $(d\sigma/dp)/\sigma_m$ . The resulting cross sections contain a systematic uncertainty of  $\sim 10\%$  introduced by this latter procedure.

### D. Transmission-loss correction

The correction for transmission loss through the spectrometer is of the form

$$\sigma(T, F) = X(\theta_F) \sigma_m(T, F), \quad (9)$$

where the correction factor  $X(\theta_F)$  depends upon the angle  $\theta_F \equiv \Gamma_1/\langle P \rangle$ ;  $\Gamma_1$  is the width of the Gaussian momentum distribution perpendicular to the beam direction and is assumed to be the same as the parallel-momentum width in the rest frame of the beam particles.<sup>15</sup> The measured momentum

widths  $\Gamma$  were corrected for the effect of the momentum size of the detector; this procedure introduced an uncertainty of  $\sim 10\%$  into the values for  $\Gamma$ . These widths then were transformed to the rest frame of the beam and were fitted with the Lepore-Riddell form<sup>15,16</sup>

$$\Gamma = \Gamma_0 [A_F(A_B - A_F)]^{1/2} / A_B, \quad (10)$$

where  $A_B$  and  $A_F$  are the projectile and fragment masses, respectively, and  $\Gamma_0$  is the fitted parameter. The values for  $\Gamma_0$  that result from this procedure, together with the measured  $\langle P \rangle$ , were used to calculate  $\theta_F$ . The correction for transmission loss is  $< 1\%$  for  $A_F \geq 15$ , but increases rapidly with decreasing  $A_F$ , so that  $X(\theta_F) = 1.77$  for  ${}^6\text{Li}$ . The uncertainty in this correction is  $\sim 10\%$  of  $[X(\theta_F) - 1]$ ; thus it is negligible for  $A_F \geq 13$ , and it is  $\sim 1\%$  for  $A_F = 12$ , but it becomes almost  $10\%$  for  $A_F = 6$ . It should be noted, however, that this uncertainty is independent of the target and hence  $\gamma_T$ , and therefore has no effect upon the electromagnetic-dissociation cross sections reported here.

The resulting  $\sigma(T, F)$  are compiled in Table III. The uncertainties listed are statistical only.

#### E. Factorization and electromagnetic-dissociation cross sections

A set of 48 values for  $\sigma(T, F)$  from eight fragments ( ${}^{15}\text{N}$ ,  ${}^{14}\text{N}$ ,  ${}^{15}\text{C}$ ,  ${}^{12}\text{C}$ ,  ${}^{12}\text{B}$ ,  ${}^{10}\text{B}$ ,  ${}^{10}\text{Be}$ , and  ${}^7\text{Li}$ ) and six targets (Be, C, Al, Ti, Pb, and U) were fitted with the form of Eq. (2) by a least-squares minimization procedure to produce the corresponding  $\gamma_T$  and  $\gamma_F$ . The  $\gamma_T$  for the targets Cu, Sn, and W were determined using the above  $\gamma_F$  from the fragments  ${}^{14}\text{N}$ ,  ${}^{12}\text{C}$ , and  ${}^{10}\text{B}$ . The  $\gamma_F$  for the electromagnetic-dissociation fragments  ${}^{17}\text{O}$ ,  ${}^{16}\text{O}$ ,  ${}^{17}\text{N}$ ,  ${}^{14}\text{C}$ , and  ${}^{13}\text{C}$  were determined with the above  $\gamma_T$  from the low- $Z$  targets Be, C, and Al.

In order to estimate the accuracy with which these factors can be used to predict  $\sigma_{\text{nuc}}$  for target-fragment combinations that have a sizable  $\sigma_{\text{em}}$ , the ratio  $\gamma = \gamma_T \gamma_F / \sigma(T, F)$  was constructed for all the cross sections and analyzed in the following way. First, the values of  $\gamma$  for the set of the 48  $\sigma(T, F)$  mentioned above were found to follow a Gaussian distribution with a mean of  $\bar{\gamma}_1 = 1.003$  and a standard deviation of  $\sigma_1 = 0.038$ . The second analysis was performed on the values of  $\gamma$  from a set of 77  $\sigma(T, F)$  which includes all of the measured  $\sigma(T, F)$  except for those of the  ${}^6\text{Li}$  fragment and for those with a sizable value for  $\sigma_{\text{em}}$ . The  $\sigma(T, F)$  with a sizable  $\sigma_{\text{em}}$  are those for the fragments  ${}^{17}\text{O}$ ,  ${}^{16}\text{O}$ ,  ${}^{17}\text{N}$ ,  ${}^{16}\text{N}$ ,  ${}^{14}\text{C}$ , and  ${}^{13}\text{C}$  with the targets Ti, Cu, Sn, W, Pb, and U. These values for  $\gamma$  were found to follow a Gaussian distribution with a mean  $\bar{\gamma}_2 = 0.996$  and a standard deviation of  $\sigma_2 = 0.044$ . From

this analysis, we conclude that the uncertainty in predicting  $\sigma_{\text{nuc}}$  for the purpose of determining  $\sigma_{\text{em}}$  from Eq. (1) is  $< 5\%$  of  $\sigma_{\text{em}}$ . The uncertainty introduced into  $\sigma_{\text{em}}$  by this is dependent in turn upon the relative sizes of  $\sigma_{\text{nuc}}$  and  $\sigma_{\text{em}}$ .

After the target and fragment factors had been determined, they were used to predict  $\sigma_{\text{nuc}}$  via Eq. (2) in order that  $\sigma_{\text{em}}$  could be obtained from Eq. (1). Folding together all of the above-mentioned uncertainties, including the factorization result, yields an overall systematic uncertainty in the values of  $\sigma_{\text{em}}$  from the Pb and U targets of  $\sim 10\%$  for  ${}^{17}\text{O}$  and  ${}^{16}\text{O}$  and  $\sim 20\%$  for  ${}^{17}\text{N}$ ,  ${}^{16}\text{N}$ ,  ${}^{14}\text{C}$ , and  ${}^{13}\text{C}$ .

## V. RESULTS

The systematic behavior of the target dependence of the fragment production cross sections is shown in Fig. 7. This is illustrated for each fragment as the ratio of the cross section for each target to the cross section for the Be target. The points labelled  $\gamma_T$ , the target factors, are the result of averaging over eight fragments. The curve shown is a fit to the  $\gamma_T$  data with the form indicated, as in Ref. 1. The points for the electromagnetic-dissociation nuclei  ${}^{17}\text{O}$ ,  ${}^{16}\text{O}$ , and  ${}^{17}\text{N}$  show a striking deviation from this curve. With the assumption of factorization (which is very good), the devia-

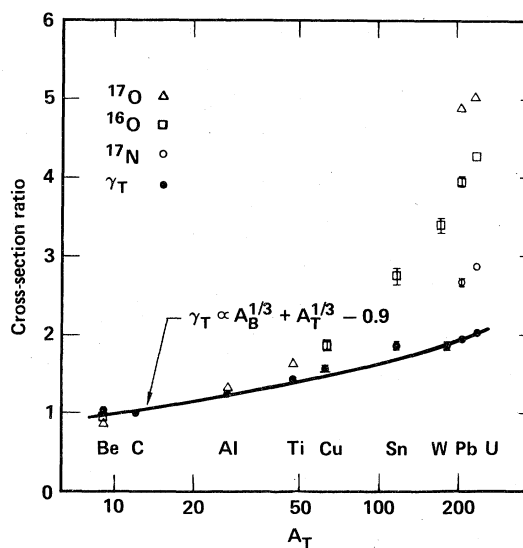


FIG. 7. Target dependence of the fragment-production cross-section ratios  $[\sigma(T, F)]/[\sigma(\text{Be}, F)]$ . The target factor  $\gamma_T$  is obtained by averaging these ratios over eight different fragments. The curve is obtained by fitting the  $\gamma_T$  points with the form  $\gamma_T \propto A_T^{1/3} + A_B^{1/3} + X$ , where  $X$  is the fitting parameter. Note the enhancement for  ${}^{17}\text{O}$ ,  ${}^{16}\text{O}$ , and  ${}^{17}\text{N}$  fragments resulting from the electromagnetic-dissociation process. The uncertainties indicated are statistical only. Systematic uncertainties are discussed in the text.



IV. Again the uncertainties listed are statistical only. The calculated predictions for the cross sections in columns JPE1 and WW contain an uncertainty from the photonuclear measurements of  $\sim 10\%$  in addition to the uncertainty caused by the differences between the two photon theories. The value of the overlap  $d$  used with the spectrum of Jäckle and Pilkuhn (JPE1) to compute the electromagnetic-dissociation cross sections is 1.5 fm, which gives the best fit to within 0.5 fm, considering the  $^{17}\text{O}$ ,  $^{16}\text{O}$ , and  $^{17}\text{N}$  data together. The corresponding value of the overlap used with the original Weizsäcker-Williams theory to give the same fit is  $-1.5$  fm.

One can consider this experiment to be a measure of the overlap  $d$ , in which case the experimental uncertainties translate into an uncertainty of  $\sim 1$  fm in  $d$ . This can be compared to the skin thickness of nuclei, which is typically  $\sim 2.2$  fm. As can be seen in Table IV, the measured values for  $\sigma_{\text{em}}$  for  $^{16}\text{O}$  are relatively larger than those for  $\sigma_{\text{em}}$  for either  $^{17}\text{O}$  or  $^{17}\text{N}$  when compared to the theory. By fitting  $d$  to each of these three electromagnetic-dissociation channels individually, we find that the overlap distance to account for  $\sigma_{\text{em}}(^{16}\text{O})$  is about 2 fm larger than that for either  $\sigma_{\text{em}}(^{17}\text{O})$  or  $\sigma_{\text{em}}(^{17}\text{N})$ . These results are shown in Table V. Because  $d$  is determined by nuclear processes (rather than by electromagnetic processes), the overlap for  $^{16}\text{O}$  is consistent with the reasonable notion that two-neutron removal from the projectile is more likely to occur with a larger overlap (smaller impact parameter) than for single-nucleon removal.

The photodissociation cross sections appropriate to  $^{16}\text{N}$ ,  $^{14}\text{C}$ , and  $^{13}\text{C}$  have not been measured; thus predictions for  $\sigma_{\text{em}}$  for these fragments cannot be calculated. In consideration of both the results of a recent measurement at Giessen<sup>17</sup> of charged photoparticles from  $^{18}\text{O}$  and those of the Livermore<sup>6</sup> measurement, the  $\sigma_{\text{em}}$  we determined are reasonable (see below).

In order to show the dependence upon  $Z_T$  of the electromagnetic-dissociation cross sections, we have plotted  $\sigma_{\text{em}}$  for  $^{17}\text{O}$ ,  $^{16}\text{O}$ , and  $^{17}\text{N}$  as functions of  $\log(Z_T)$  in Fig. 8. The lines drawn are the predictions given by the calculation of Jäckle and Pilkuhn<sup>9</sup> from Table IV, JPE1. By fitting the  $Z_T$  dependence of the  $^{16}\text{O}$  cross sections, we find that  $\sigma_{\text{em}}(T, ^{16}\text{O}) \propto Z_T^{1.87 \pm 0.15}$ , in agreement with the theoretical value of  $Z_T^{1.8}$  given in Eq. (3).

## VI. DISCUSSION

The main feature to be noticed from the results of this experiment is that the enhancement of the fragmentation cross sections for  $^{18}\text{O}$  projectiles

TABLE V. Best-fit overlap values (mb).

Fragment	$d^{a,b}$	
	JPE1	WW
$^{17}\text{O}$	1.0	-2.5
$^{16}\text{O}$	2.5	-0.5
$^{17}\text{N}$	0.5	-3.0
weighted <sup>c</sup> average	1.5	-1.5

$$^a d \equiv R_{0.1}(T) + R_{0.1}(B) - b_{\text{min}}.$$

<sup>b</sup> These values are calculated to the nearest 0.5 fm.

<sup>c</sup> Weighted by the inverse square of the error bar for each value of  $\sigma_{\text{em}}$ .

with high- $Z$  targets in a channel corresponding to an appreciable photonuclear cross section is described very well by the electromagnetic-dissociation process, in terms of both magnitude and dependence upon  $Z_T$ . Given a conservative estimate for the experimental uncertainties, the relative sizes of the electromagnetic-dissociation cross sections  $\sigma_{\text{em}}(T, ^{17}\text{O})$ ,  $\sigma_{\text{em}}(T, ^{16}\text{O})$ , and  $\sigma_{\text{em}}(T, ^{17}\text{N})$  are consistent with predictions using the measured photonuclear cross sections. However, the fact that the cross section for  $^{16}\text{O}$  is relatively larger than those for  $^{17}\text{O}$  and  $^{17}\text{N}$  indicates that the effective impact parameter for the nuclear processes that produce  $^{16}\text{O}$  might very well be smaller than that for the production of either  $^{17}\text{O}$  or  $^{17}\text{N}$ .

The Giessen experiment<sup>17</sup> on  $^{18}\text{O}$  suggests that

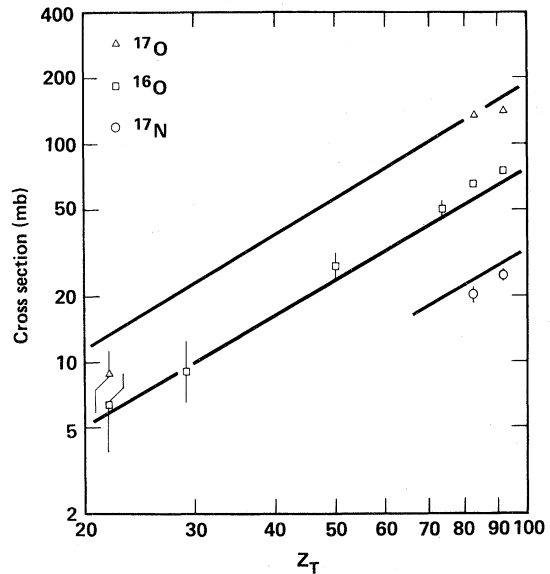


FIG. 8. Electromagnetic-dissociation cross section  $\sigma_{\text{em}}$  vs  $\log(Z_T)$ . The curves are the calculated predictions from Table III. The uncertainties indicated are statistical only. Systematic uncertainties are discussed in the text.

we should see a small amount of  $^{16}\text{N}$ , which, in fact, we do. They also made a measurement of the  $^{18}\text{O}(\gamma, \alpha_0)^{14}\text{C}$  cross section, at photon energies  $E_\gamma > 19$  MeV, which does not have enough strength to produce the amount of  $^{14}\text{C}$  that we see. However, because of the low threshold for the  $^{18}\text{O}(\gamma, \alpha)$  reaction ( $E_\gamma = 6.23$  MeV), such cross section as exists for  $E_\gamma < 19$  MeV (not measured in the Giessen experiment) is greatly enhanced by the energy dependence of the virtual-photon spectrum (see Fig. 2). Also, the Livermore measurement<sup>5</sup> indicates that there might be some strength in transitions to excited states in  $^{14}\text{C}$  which also is not included in the Giessen data. Therefore, we expect to see considerably more  $^{14}\text{C}$  production than that attributable alone to the  $(\gamma, \alpha_0)$  cross section above 19 MeV. Also, considering the relatively low threshold for the  $^{18}\text{O}(\gamma, \alpha n)^{13}\text{C}$  reaction ( $E_\gamma = 14.4$  MeV), which is only 2.2 MeV higher than the  $^{18}\text{O}(\gamma, 2n)$  threshold, we are not surprised at the magnitude of  $\sigma_{\text{em}}$  for the production of  $^{13}\text{C}$ .

The question of factorization of nuclear cross sections embodied in Eq. (2) is a topic in itself and is not treated extensively here. We merely want to state our very significant result that factorization is valid to an accuracy of better than 4%. This limit is smaller by a factor of 4 than the previous experimental result of Ref. 8.

Having established that the electromagnetic-dissociation process is the correct mechanism for the enhancement in fragment-production cross sections for high- $Z$  targets where the photonuclear

cross sections are large, it can be seen that this type of experiment provides information on all of the photodissociation channels simultaneously. The quality of this information, however, would be enhanced significantly by a better treatment of the virtual-photon theory; the difference between the two theories<sup>9-11</sup> with a point-charge target is particularly annoying.

The acquisition of information about all of the photoreaction channels simultaneously is a unique feature of this method. Another unique feature of the method is that it permits the measurement of the photoreaction channels of *unstable* nuclei with lifetimes as short as  $\sim 10$  ns, by the use of secondary beams of  $\beta$ -unstable nuclei; this in turn expands by a large factor the number of nuclei (especially light nuclei) available for photonuclear studies.

#### ACKNOWLEDGMENTS

We extend our thanks to L. W. Burr for her conscientious help with the data analysis. We are grateful to Y. J. Karant for fruitful discussions on factorization and to A. Goldberg and T. W. Donnelly for a critical reading of the manuscript. This work was performed under the auspices of the U. S. Department of Energy under Contract No. W-7405-ENG-48 (LLL, LBL) and the National Aeronautics and Space Administration under Grant No. NGR 05-003-513.

<sup>1</sup>H. H. Heckman and P. J. Lindstrom, Phys. Rev. Lett. **37**, 56 (1976).

<sup>2</sup>G. D. Westfall, L. W. Wilson, P. J. Lindstrom, H. J. Crawford, D. E. Greiner, and H. H. Heckman, Phys. Rev. C **19**, 1309 (1979).

<sup>3</sup>Electromagnetic dissociation at relativistic energies is the same process that has been described previously with the name Coulomb dissociation (see Refs. 1, 2, 4, 5, 9). Within the nuclear-physics community, the term Coulomb implies a longitudinal photon process, whereas this process is dominated by transverse photons. In order to minimize confusion, we have chosen to use the name electromagnetic dissociation.

<sup>4</sup>G. Fäldt, Phys. Rev. D **2**, 846 (1970).

<sup>5</sup>X. Artru and G. B. Yodh, Phys. Lett. **40B**, 43 (1972).

<sup>6</sup>J. G. Woodworth, K. G. McNeill, J. W. Jury, R. A. Alvarez, B. L. Berman, D. D. Faul, and P. Meyer, Phys. Rev. C **19**, 1667 (1979).

<sup>7</sup>W. R. Frazer, L. Ingber, C. H. Mehta, C. H. F. n., D. Silverman, K. Stowe, P. D. Ting, and H. J. Yesian, Rev. Mod. Phys. **44**, 284 (1972).

<sup>8</sup>P. J. Lindstrom, D. E. Greiner, H. H. Heckman, B. Cork, and F. S. Bieser, Lawrence Berkeley Labora-

tory Report No. LBL-3650, 1975 (unpublished).

<sup>9</sup>R. Jäckle and H. Pilkuhn, Nucl. Phys. **A247**, 521 (1975).

<sup>10</sup>J. D. Jackson, *Classical Electrodynamics* (Wiley, New York, 1975), 2nd ed., p. 719.

<sup>11</sup>H. Pilkuhn, private communication to H. Heckman.

<sup>12</sup>R. Hofstadter and H. R. Collard, in *Landolt-Bornstein: Numerical Data and Functional Relationships in Science and Technology*, edited by H. Schopper (Springer, Berlin, 1967), Group I, Vol. 2, p. 21.

<sup>13</sup>I. Angeli and M. Csatlos, Nucl. Phys. **A288**, 480 (1977).

<sup>14</sup>H. Miska, B. Norum, M. V. Hynes, W. Bertozzi, S. Kowalski, F. N. Rad, C. P. Sargent, T. Sasanuma, and B. L. Berman, Phys. Lett. **83B**, 165 (1979).

<sup>15</sup>D. E. Greiner, P. J. Lindstrom, H. H. Heckman, B. Cork, and F. S. Bieser, Phys. Rev. Lett. **35**, 152 (1975).

<sup>16</sup>J. V. Lepore and R. J. Riddell, Jr., Lawrence Berkeley Laboratory Report No. LBL-3086, 1974 (unpublished).

<sup>17</sup>K. Bangert, U.E.P. Berg, G. Junghans, R. Stock, and K. Wienhard, Nucl. Phys. A (to be published).